Magnetic and orbital order in $(R\mathrm{MnO_3})_n/(A\mathrm{MnO_3})_{2n}$ superlattices studied via a double-exchange model with strain

Shuai Dong,[1,2,3,4] Qinfang Zhang,[5,6,7] Seiji Yunoki,[6,7,8] J.-M. Liu,[4,9] and Elbio Dagotto[2,3]

[1]*Department of Physics, Southeast University, Nanjing 211189, China*

[2]*Department of Physics and Astronomy, University of Tennessee, Knoxville, Tennessee 37996, USA*

[3]*Materials Science and Technology Division, Oak Ridge National Laboratory, Oak Ridge, Tennessee 37831, USA*

[4]*National Laboratory of Solid State Microstructures, Nanjing University, Nanjing 210093, China*

[5]*Key Laboratory for Advanced Technology in Environmental Protection of Jiangsu Province, Yancheng Institute of technology, Yancheng 224051, China*

[6]*Computational Condensed Matter Physics Laboratory, RIKEN ASI, Wako, Saitama 351-0198, Japan*

[7]*CREST, Japan Science and Technology Agency (JST), Kawaguchi, Saitama 332-0012, Japan*

[8]*Computational Materials Science Research Team, RIKEN AICS, Kobe, Hyogo 650-0047, Japan*

[9]*International Center for Materials Physics, Chinese Academy of Sciences, Shenyang 110016, China*

(Received 17 September 2012; published 19 November 2012)

The two-orbital double-exchange model is employed for the study of the magnetic and orbital orders in $(R\mathrm{MnO_3})_n/(A\mathrm{MnO_3})_{2n}$ (R: rare earths; A: alkaline-earth metal) superlattices. The A-type antiferromagnetic order is observed in a broad region of parameter space for the case of $SrTiO_3$ as substrate, in agreement with recent experiments and first-principles calculations using these superlattices. In addition, a C-type antiferromagnetic state is also predicted to be stabilized when using substrates like $LaAlO_3$ with smaller lattice constants than $SrTiO_3$, again in agreement with first-principles results. The physical mechanism for the stabilization of the A and C magnetic transitions is driven by the orbital splitting of the $x^2 - y^2$ and $3z^2 - r^2$ orbitals. This splitting is induced by the Q_3 mode of Jahn-Teller distortions created by the strain induced by the substrates. In addition to the special example of $(LaMnO_3)_n/(SrMnO_3)_{2n}$, our phase diagrams can be valuable for the case where the superlattices are prepared employing narrow bandwidth manganites. In particular, several nonhomogenous magnetic profiles are predicted to occur in narrow-bandwidth superlattices, highlighting the importance of carrying out investigations in this mostly unexplored area of research.

DOI: 10.1103/PhysRevB.86.205121 PACS number(s): 71.30.+h, 73.21.Cd, 75.47.Lx

I. INTRODUCTION

In recent years, remarkable progress has been achieved in the experimental and theoretical study of complex oxide heterostructures. At present, atomic-scale smooth interfaces involving pairs of oxides with similar crystal structures and lattice constants can be routinely synthesized and characterized with sophisticated techniques, potentially leading to a variety of interesting electronic devices.[1–7] As a prototype of correlated electron systems, manganites have been widely involved in complex oxides heterostructures (e.g., manganite-cuprate,[8,9] manganite-titanate,[10] manganite-nickelate,[11] and manganite-$BiFeO_3$).[12] Even pure manganite-manganite superlattices made by antiferromagnetic insulators $LaMnO_3$ (LMO) and $SrMnO_3$ (SMO) are quite nontrivial.[13–24] A metal-insulator transition was observed with increasing n for the case of $(LaMnO_3)_{2n}/(SrMnO_3)_n$ superlattices,[17,18,20] with LMO to SMO in proportion of 2 to 1. Both employing microscopic models and density-functional theory (DFT) calculations, the presence of magnetic modulations in these superlattices have been reported, which may be responsible for the metal-insulator transition.[25,26]

Recently, May *et al.* observed an enhanced Néel temperature of the A-type antiferromagnetic (A-AFM) order in the $(LaMnO_3)_n/(SrMnO_3)_{2n}$ ($n = 1, 2$) superlattices,[21] where now the LMO and SMO are in proportion of 1 to 2. This is surprising since from the theory perspective it is not straightforward to understand the presence of a uniform A-AFM order because previous theoretical studies (using both model and DFT approaches) predicted that the ground-state spin order within the $SrMnO_3$ region was G-type antiferromagnetic (G-AFM) even when there were only two consecutive SrO sheets as in the case of $(LaMnO_3)_4/(SrMnO_3)_2$.[25,26] In the $(LaMnO_3)_n/(SrMnO_3)_{2n}$ superlattices, the consecutive SrO sheets can reach up to 4 when $n = 2$. Thus, the e_g electron density deep within this $SrMnO_3$ region is expected to be very close to zero as in the case of bulk $SrMnO_3$. For such a low electronic density, typically the G-AFM order is robust and the A-AFM order would be unusual according to the corresponding phase diagrams for bulk compounds.[27] However, contrary to these expectations, the experiments of May *et al.* unveiled a robust A-AFM order which was uniform *all through* the superlattices without any noticeable magnetic modulation.[21] Thus, it is very important to perform better-refined theoretical studies to understand this puzzling behavior.

Very recently, some of the authors performed a DFT calculation that actually confirmed the presence of a nearly uniform A-AFM phase for the case of $(LaMnO_3)_n/(SrMnO_3)_{2n}$ when using $SrTiO_3$ (STO) as a substrate and employing an on-site Hubbard U repulsion not too large (e.g., $U < 1.5$ eV).[28] Furthermore, a uniform C-type antiferromagnetic (C-AFM) order was predicted to occur for these superlattices for the case of a $LaAlO_3$ (LAO) substrate also for $U < 1.5$ eV.[28] In this previous DFT study, the effect of strain was emphasized to tune the orbital and magnetic orders. The role of strain to stabilize A-AFM and C-AFM phases for $La_{1-x}Sr_xMnO_3$ thin film and

$(LaMnO_3)_1/(SrMnO_3)_1$ superlattice was also discussed before from the perspective of DFT calculations.[29,30]

In the present paper, the $(RMnO_3)_n/(AMnO_3)_{2n}$ superlattices will be revisited now using the two-orbital double-exchange model, as opposed to a first-principles study. Our mission is not only to confirm (or refute) the DFT predictions from a conceptually different perspective, but also to reveal in more detail the physical mechanisms behind the results, particularly with regards to the relationship between magnetism and orbital population. Furthermore, our model calculations can go beyond $(LaMnO_3)_n/(SrMnO_3)_{2n}$ and shed light on generic narrow-bandwidth $(RMnO_3)_n/(AMnO_3)_{2n}$ superlattices which have not been experimentally prepared thus far and which are difficult to analyze accurately with DFT methods. Our study confirms the presence of the A-AFM and C-AFM states, in good agreement with DFT, but it has also unveiled a plethora of other phases, including exotic states with nonuniform configurations, which potentially can emerge in narrow-bandwidth superlattices after the appropriate selection of elements in the chemical formula and of the substrate.

The organization of the paper is as follows: In Sec. II, the model and the method used are presented, with a discussion of the profile of the electrostatic potential used for the superlattices as well as the variational states employed. The importance of using twisted boundary conditions, particularly for the A-AFM and C-AFM phases, is discussed in this section as well. Section III contains the main results and specific conclusions for the cases of the two substrates STO and LAO under study here. Emphasis is given to phase diagrams varying the superexchange and the electrostatic potential strength. Also in this section, the orbital occupation and electronic density for the many layers are discussed, as well as the implications of our results for more narrow-bandwidth manganites. A summary is provided in Sec. IV.

II. MODEL, METHOD, AND BOUNDARY CONDITIONS

In this investigation, the standard two-orbital double-exchange model will be employed in the widely used limit of an infinite Hund coupling for simplicity. Work carried out over several decades by dozens of groups has repeatedly shown that this double-exchange model provides a realistic starting approximation for manganite compounds.[31–33] More explicitly, the model Hamiltonian is given by

$$H = -\sum_{\langle ij\rangle}^{\alpha\beta} t_{\alpha\beta}^{\vec{r}}(\Omega_{ij} c_{i\alpha}^{\dagger} c_{j\beta} + \text{H.c.}) + J_{\text{AFM}} \sum_{\langle ij\rangle} \vec{S}_i \cdot \vec{S}_j + \lambda \sum_i Q_{3i}\tau_{zi} + \sum_i V_i n_i. \quad (1)$$

In this Hamiltonian, the first term represents the standard double-exchange hopping process for the e_g electrons. The operators $c_{i\alpha}$ ($c_{i\alpha}^{\dagger}$) annihilate (create) an e_g electron at the orbital α of lattice site i. The spin index is no longer necessary since the spin of the e_g electrons is always parallel to the localized t_{2g} spin $\vec{S}_i$ due to the infinite Hund coupling approximation. The three nearest-neighbor (NN) hopping directions are denoted by $\vec{r}$. The Berry phase Ω_{ij} generated by the infinite Hund coupling approximation equals $\cos(\theta_i/2)\cos(\theta_j/2) + \sin(\theta_i/2)\sin(\theta_j/2)\exp[-i(\phi_i - \phi_j)]$, where θ and ϕ are the polar and azimuthal angles of the t_{2g} spins, respectively, and i and j are NN sites. Two e_g orbitals (a: $d_{x^2-y^2}$ and b: $d_{3z^2-r^2}$) are involved in the double-exchange process for manganites, with the hopping amplitudes given by

$$t^x = \begin{pmatrix} t_{aa}^x & t_{ab}^x \\ t_{ba}^x & t_{bb}^x \end{pmatrix} = \frac{t_0}{4}\begin{pmatrix} 3 & -\sqrt{3} \\ -\sqrt{3} & 1 \end{pmatrix},$$
$$t^y = \begin{pmatrix} t_{aa}^y & t_{ab}^y \\ t_{ba}^y & t_{bb}^y \end{pmatrix} = \frac{t_0}{4}\begin{pmatrix} 3 & \sqrt{3} \\ \sqrt{3} & 1 \end{pmatrix}, \quad (2)$$
$$t^z = \begin{pmatrix} t_{aa}^z & t_{ab}^z \\ t_{ba}^z & t_{bb}^z \end{pmatrix} = t_0\begin{pmatrix} 0 & 0 \\ 0 & 1 \end{pmatrix}.$$

Below, in the presentation of our results, t_0 will be considered as the unit of energy. The second term of the Hamiltonian is the antiferromagnetic superexchange (SE) interaction between the NN t_{2g} spins. The typical value of the SE coupling J_{AFM} is approximately between $0.05t_0$ and $0.1t_0$, based on a variety of previous investigations for bulk manganites.[25,31–33] The third term stands for the electron-lattice interaction, with λ being a dimensionless coupling. A crucial aspect of the present investigation is the inclusion of the strain caused by the substrate. This strain is here modeled using the Q_3 [$\sim(2\delta_z - \delta_x - \delta_y)$] mode of the Jahn-Teller (JT) distortions, where δ_α stands for the change in the length of the O-Mn-O bonds along a particular axis α. The operator τ_z ($=c_a^{\dagger}c_a - c_b^{\dagger}c_b$) is an orbital pseudospin operator. The term $\lambda Q_3\tau_z$ splits the energy levels of the orbitals $d_{x^2-y^2}$ and $d_{3z^2-r^2}$.

From a formal perspective, the double-exchange hopping amplitudes, as well as the superexchange and Jahn-Teller couplings, may be different at the $RMnO_3$ and $AMnO_3$ regions, and at the interface. However, since the in-plane lattice constants are fixed to those of the substrate by the growing process, then the in-plane interaction couplings will be considered almost uniform all through the superlattices. With regards to the out-of-plane coupling strengths, in principle they should take different values for $RMnO_3$, $AMnO_3$, and the interface. However, to fully consider these effects additional parameters are needed since their precise values are not available in the current state of investigations in oxide superlattices. Thus, in order to avoid having too many free parameters, it is a practical choice to carry out these investigations assuming uniform couplings, as used in previous work.[25,34,35] This approximation reduces the numbers of model parameters needed in our study, allowing us to focus on the most important aspects of the physics of the problem.[25,34,35]

In our study neither the breathing mode Q_1 nor the JT mode Q_2 are considered in the calculations for the following reasons: First, the contribution that arises from Q_1, which effectively modifies the on-site potential, can be simply merged into the fourth term. Second, with regards to the Q_2 JT mode, its average value $\langle Q_2\rangle$ is zero if the substrate is biaxially isotropic. Although the local values of Q_{2i} may become nonzero in special cases such as for the undoped manganites $RMnO_3$ with orbital order,[36] the Q_{2i} profile is not considered important in the bulk doped manganites such as $R_{1/3}A_{2/3}MnO_3$[37] and, more importantly for our studies on superlattices, they have not been reported as being of relevance in previous studies of $(RMnO_3)_n/(AMnO_3)_{2n}$ superlattices to our knowledge.

TABLE I. Parameter profiles used in the present simulations. Upper rows: the value of Q_{3i}s in the three regions of relevance, for the two substrates considered here; namely, for MnO_2 layers in between two RO layers (represented as RMnO$_3$), in between an RO layer and an AO layer (represented as $R_{1/2}A_{1/2}$MnO$_3$), and finally in between two AO layers (represented as AMnO$_3$). The lattice constants of RMnO$_3$ and SrTiO$_3$ are similar, while those of AMnO3 and LaAlO$_3$ are also similar. Here Q is positive. Lower row: value of V_i in the three regions.

Q_{3i}	RMnO$_3$	$R_{1/2}A_{1/2}$MnO$_3$	AMnO$_3$
SrTiO$_3$	0	$-Q/2$	$-Q$
LaAlO$_3$	Q	$Q/2$	0
V_i	0	$V/2$	V

Therefore, the Q_{2i} term will be neglected in the present effort for mere simplicity.

In our calculations, Q_{3i} is proportional to the local quantity $(c/a - 1)$, where c and a are the out-of-plane and in-plane lattice constants, respectively. The specific generic values of Q_{3i} used in the present work are listed in Table I. In the present effort, the superlattices are assumed to be fully strained following the underlying substrates, as observed experimentally.[21]

The fourth term is the on-site Coulomb potential energy, and n_i is the local e_g electronic density. V_i is the Coulomb potential arising from the A-site cations, from the e_g electrons, and from the oxygen anions (i.e., the Q_1 mode distortion mentioned before). In the rest of the paper, the profile of V_i will be approximately determined by the NN A-site cations,[25,38] as shown in Table I, while its actual magnitude V will be considered a parameter and phase diagrams will be constructed varying this parameter. Fixing such a profile is not a drastic approximation since previous more-detailed studies, even using the self-consistent Poisson equation, have shown that these sophisticated approaches tend to produce smooth potentials with profiles similar to those used here.[35] For the benefit of the reader, the distribution of the MnO_2, RO, and AO layers present in our superlattices are shown in Fig. 1.

The above-described model Hamiltonian has been numerically solved here using finite clusters. To simulate the case of the $(R\text{MnO}_3)_n/(A\text{MnO}_3)_{2n}$ ($n = 1, 2$) superlattices, a $4 \times 4 \times 6$ cluster with twisted boundary conditions (TBCs)[39] is here adopted. The TBC with proper k meshes ($k \times k \times k$ used here) are often employed to reach larger lattices, thus reducing the finite-size lattice effects (which are indeed of relevance in the present study, as shown below).[40]

To determine the ground-state phases in these superlattices, a variational procedure is used; namely, the energies of candidate phases are compared in the J_{AFM}-V parameter space, for several values of λQ_3 as an additional parameter. The candidate phases are proposed according to the symmetries of the superlattices. Contrary to other variational studies limited to a relatively small number of proposed states, in this effort 30 candidates for the $n = 1$ case and 56 candidates for the $n = 2$ case have been considered. These candidate states were constructed by combining the well-known FM, A-AFM, C-AFM, and G-AFM spin arrangements in each of the layers (note that the CE-AFM state is not considered since the Q_2 mode is neglected). Some of these candidates will appear explicitly in the phase diagrams described below in Sec. III, and some of them are presented in Fig. 2 for the benefit of the reader.

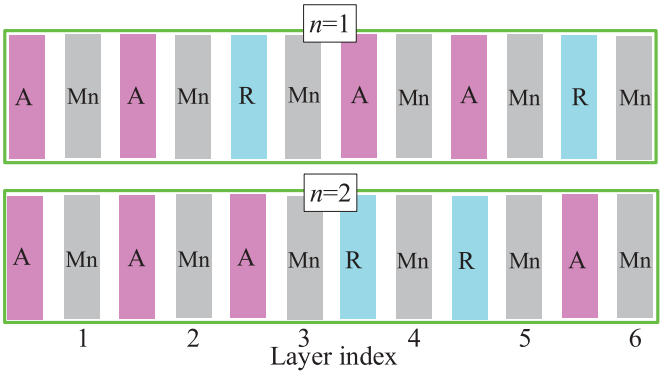

FIG. 1. (Color online) Sketch showing the distribution of layers in the finite cluster with six Mn-oxide layers used in our studies. "Mn" stands for the MnO_2 layers, "R" for the RO layers, and "A" for the AO layers. The only active layers for the mobile electrons are the Mn layers in our study, but the other layers influence on the Mn layers by their electrostatic potential, as discussed in the text and shown in Table I.

A. Discussion of finite-size lattice effects

In several previous computational studies of the double-exchange model, periodic boundary conditions (PBCs) were used for Monte Carlo simulations carried out in real-space lattices.[25] Due to the substantial CPU-time consumed by the frequent diagonalizations in the fermionic sector, calculations have been typically limited to relatively small lattice sizes, especially for three-dimensional studies. For example, in several cases the in-plane lattice cell was only 4×4 in size,[25,35,41] which might give rise to non-negligible finite-size effects. These effects are not very prominent for the ferromagnetic (FM), G-AFM, or even the CE-type antiferromagnetic cases, which were analyzed in previous studies.[25,35,41] However, as will be described below, in the effort described here the dominant states involved are the A-AFM and C-AFM phases in various combinations. It is necessary to verify that the finite-size lattice effects are not too large for these phases. Moreover, the presence of a superlattice structure may increase the relevance of these effects.

This present study of size effects and boundary conditions will be carried out first without the superlattice structure; namely, mimicking the bulk system. The conclusions of this subsection will then be applied to the superlattice study in the rest of the paper. In Figs. 3(a) and 3(b), the ground-state energies (per site) of the FM, A-AFM, and C-AFM phases are calculated for the case of bulk $R_{1/3}A_{2/3}$MnO$_3$ using the above-described Hamiltonian (and with $Q_{3i} = 0$ and $V_i = 0$, for simplicity; i.e., no superlattice is considered in this test, as already explained). The energies of these three states are compared for both the cases of PBC and TBC. In the PBC case, the ground state changes from FM to A-AFM, and then to C-AFM with increasing superexchange J_{AFM} (or equivalently by decreasing the overall bandwidth). As shown in Fig. 3(a),

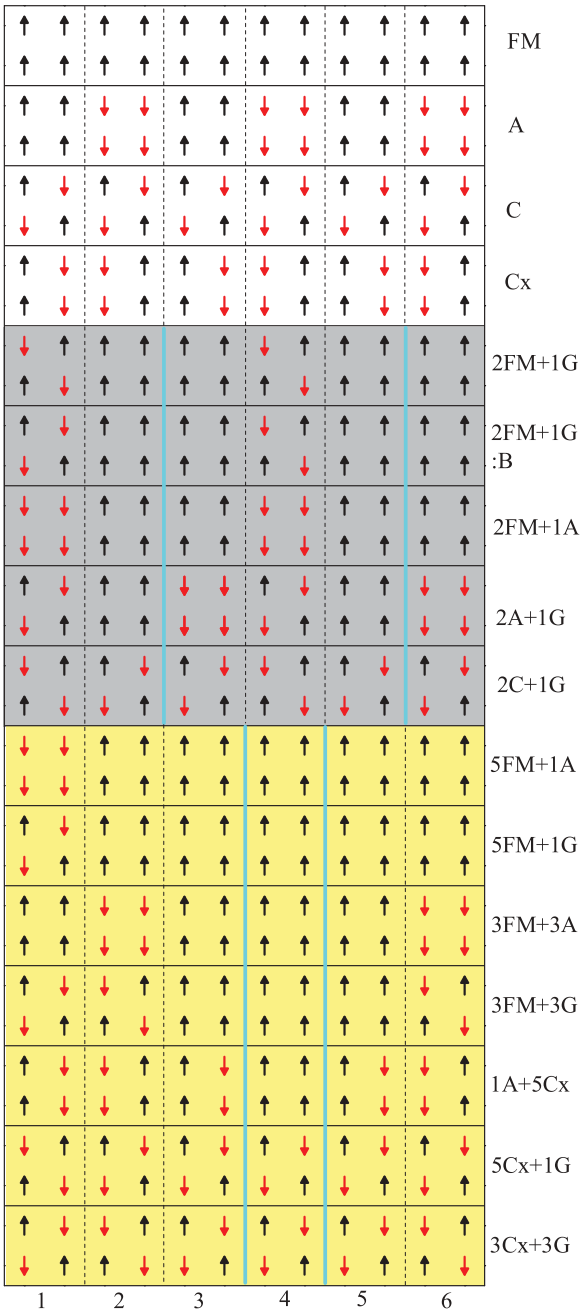

FIG. 2. (Color online) Sketch of the spin patterns for several of the variational states considered here. The index for the six layers of MnO_2 in our finite-cluster study is shown at the bottom. In this figure, only a 2×2 unit for each layer is shown. The rest of the magnetic state at each layer is obtained by repeating the pattern provided. The first four configurations (i.e., those with the white background) are uniform and common for the $n = 1$ and $n = 2$ cases. States of this kind also appear in the bulk limit and are not affected by the superlattice periodicity. The next five configurations shown (with the gray background) are only for the $n = 1$ case. The last seven configurations (with the yellow background) are only for the $n = 2$ case. In the nonuniform cases, the cyan bars indicate the location of the RO sheets (while the AO sheets are not shown explicitly). The nonuniform phases are denoted using a notation $mX + m'Y$, where X and Y are abbreviations for the X-AFM and Y-AFM phases, and m/m' are the fractions of the X/Y phases, respectively.

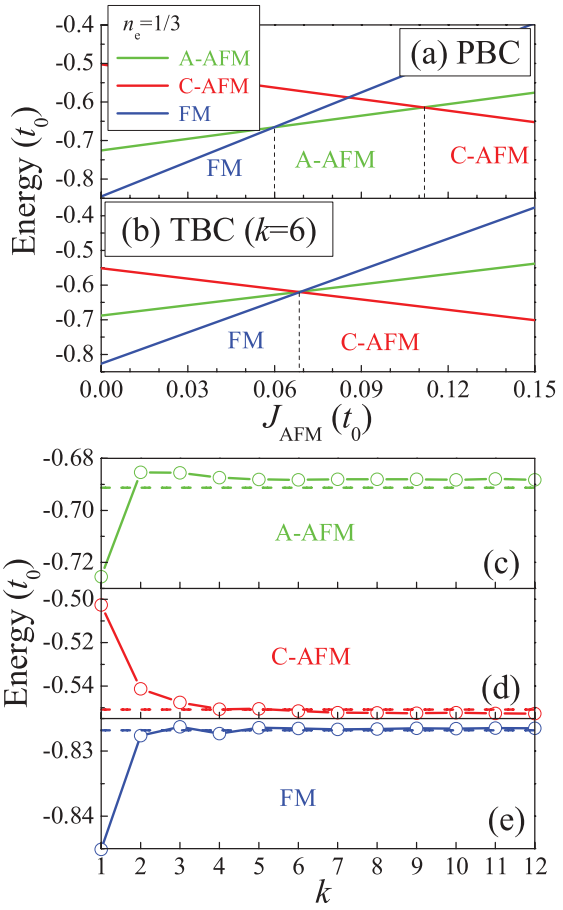

FIG. 3. (Color online) Comparison of energies using a $4 \times 4 \times 6$ lattice (without including the JT distortion Q_{3i} and the Coulomb potential V_i, for simplicity) contrasting the cases of the PBC and the TBC. The overall e_g-electron density is chosen as $n_e = 1/3$. Panels (a) and (b) show the total energies (i.e., double exchange and superexchange) per site as a function of the superexchange coupling. Panel (a) is for PBC, while panel (b) is for TBC with $k = 6$. The "coincidence" of the three energies in panel (b) at one particular value of J_{AFM} is accidental. (c)–(e) Double-exchange energy for each of the cases indicated, as a function of k in the TBC mesh. The accurate energies for the bulk limit obtained analytically[42] are also shown as dashed lines to guide the eye. It is obvious that the use of TBC can drastically reduce the finite-size effects.

with these boundary conditions the A-AFM state is stable from $J_{AFM} = 0.06$ to $J_{AFM} = 0.11$. However, the A-AFM state is actually unstable with the use of the TBC, and the ground state changes from FM to C-AFM directly, as shown in Fig. 3(b), with the A-AFM coexisting with the other two states at just one point. Therefore, to reduce this finite-size lattice effect, the TBC will be adopted in the rest of the calculations described here. However, note that the use of TBC considerably increases the CPU time of the study, which renders a fully unbiased Monte Carlo simulation too time consuming. However, our use of dozens of variational states gives us confidence that the present results have captured the essence of the problem.

In Figs. 3(c) and 3(d), the double-exchange energies (per site) are shown as a function of the value of k in the TBC. From the energy values in the vertical axes, it is clear that the per-site energy deviation from the bulk value using the

PBC (corresponding to $k = 1$) is the most serious for the case of the C-AFM state (up to $-0.05t_0$), milder for the A-AFM state (up to $0.037t_0$), and the less important for the FM state (difference less than $0.019t_0$). And, moreover, $k = 6$ or even less in the TBC is certainly enough for the energy per site to overcome those finite-size lattice effects. Thus, this value of k will be adopted in the calculations for the superlattices presented below.

III. RESULTS AND DISCUSSION

A. (RMnO$_3$)$_n$/(AMnO$_3$)$_{2n}$ on SrTiO$_3$

As explained in the introduction, the results of our investigations will be provided for two particular substrates, starting with SrTiO$_3$. For this case, note that the average lattice constant for a pseudocubic RMnO$_3$ (R = La, Pr, Nd) is close to the lattice constant of SrTiO$_3$ (3.905 Å). More specifically, this (average) lattice constant is about 3.94 Å for R = La, 3.916 Å for R = Pr, and 3.907 Å for R = Nd.[43] Then, in the numerical simulations to describe this particular case, the RMnO$_3$ layers grown on SrTiO$_3$ are assumed to be nearly cubic; namely, the value $Q_{3i} = 0$ is used for the active JT mode in our study. In contrast, the cubic AMnO$_3$ has a much smaller lattice constant, in particular 3.805 Å for A = Sr and 3.727 Å for A = Ca,[44] which gives rise to an important in-plane expansion and out-of-plane reduction of the lattice constants when growing on the SrTiO$_3$ substrate. The ratio c/a of AMnO$_3$ on SrTiO$_3$ will be smaller than 1, implying a negative Q_{3i}. Therefore, in the following simulations with SrTiO$_3$ as the substrate, the values of the Q_{3i} variables are considered to be 0 in the RMnO$_3$ region (more specifically, when a MnO$_2$ layer is in between two RO layers), but $-Q$ in the AMnO$_3$ region (i.e., when the MnO$_2$ layer is in between two AO layers), where Q is a positive parameter to be tuned in our study. For the interfacial RO-MnO$_2$-AO layer, an average value $-Q/2$ is used as a first-order approximation, as shown in Table I.

The DFT results[26,28] on (LaMnO$_3$)$_{2n}$/(SrMnO$_3$)$_n$ and (LaMnO$_3$)$_n$/(SrMnO$_3$)$_{2n}$ superlattices (n = 1, 2) have indicated that the Coulomb energy difference between LaMnO$_3$ and SrMnO$_3$ is about 0.7–1 eV, which corresponds to $1.4t_0$–$2t_0$ in our simulation if t_0 is 0.5 eV (a reasonable approximate value for wide bandwidth manganites).[25] However, besides the Coulomb potential from the A-site cations, the V_i used here also contains other contributions, such as those from the breathing phononic Q_1 mode. In fact, previous model studies found that $V_i = 0.6t_0$–$0.9t_0$ is a proper range for this potential in the double-exchange model.[25] However, for completeness here the full range of V up to $2t_0$ will be investigated in the phase diagrams.

The ground-state phase diagrams corresponding to (RMnO$_3$)$_1$/(AMnO$_3$)$_2$ (n = 1) using SrTiO$_3$ as the substrate are shown in Fig. 4 at various values of λQ. Without the JT distortion [i.e., for $\lambda Q = 0$, see Fig. 4(a)], the A-AFM phase is *not* stable in this superlattice despite varying the parameters $J_{\rm AFM}$ and V. Instead, FM tendencies dominate with at most just 1/3 of the superlattice being G-AFM even at the largest $J_{\rm AFM}$ studied here. The presence of one G-AFM layer for every two FM layers is in agreement with the naive intuition described

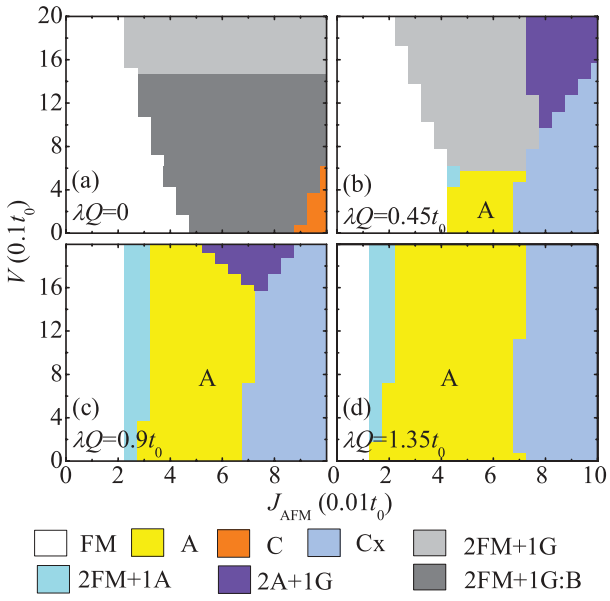

FIG. 4. (Color online) Phase diagram for the case of (RMnO$_3$)$_1$/(AMnO$_3$)$_2$ with SrTiO$_3$ as substrate, at several values of λQ.

in the introduction; namely, that the G-AFM state should be favored inside AMnO$_3$. However, these results change qualitatively when the strain effects are incorporated. In fact, with increasing λQ, the A-AFM phase now emerges around $J_{\rm AFM} = 0.05t_0$–$0.06t_0$ and takes over an increasing fraction of parameter space with increasing λQ. This effect is the most prominent in the absence of the electrostatic potential. In principle, a strong Coulomb potential V, which reduces the e_g electronic density in the AMnO$_3$ region, can suppress this uniform A-AFM order. In fact, in Fig. 4(b) the A-AFM phase is suppressed rapidly with increasing V. However, in spite of this negative influence of V, when the JT distortion is strong enough (e.g., $\lambda Q \geqslant 0.9t_0$), the A-AFM phase is stable and quite robust in the broad region of parameter space investigated here, in agreement with the experiments described in the introduction. Note also the appearance of additional robust states with further increasing $J_{\rm AFM}$, particularly the Cx state. As discussed later in the paper, these states could appear in manganites with a bandwidth smaller than for the case A = Sr.

For the case of the (RMnO$_3$)$_2$/(AMnO$_3$)$_4$ superlattice with SrTiO$_3$ as substrate, the strong JT distortion is even more crucial to obtain the A-AFM phase, as shown in Fig. 5. The A-AFM phase is stable only in the interval $J_{\rm AFM} = 0.05t_0$–$0.06t_0$ for the cases of a strong JT distortion and weak to intermediate Coulomb potentials. Comparing with the previously described case of n = 1, the A-AFM phase appears to be more fragile in the n = 2 case, with stability regions in parameter space that are smaller in size for n = 2 than for n = 1. This tendency is in agreement with the experimental results reporting that the A-AFM Néel temperature of (LaMnO$_3$)$_1$/(SrMnO$_3$)$_2$ is higher than (LaMnO$_3$)$_2$/(SrMnO$_3$)$_4$.[21] The physical reason is that the charge density deep into the AMnO$_3$ region is very low due to the Coulomb potential V. Thus, the combination of three FM layers (RMnO$_3$ and interfacial layers) plus three

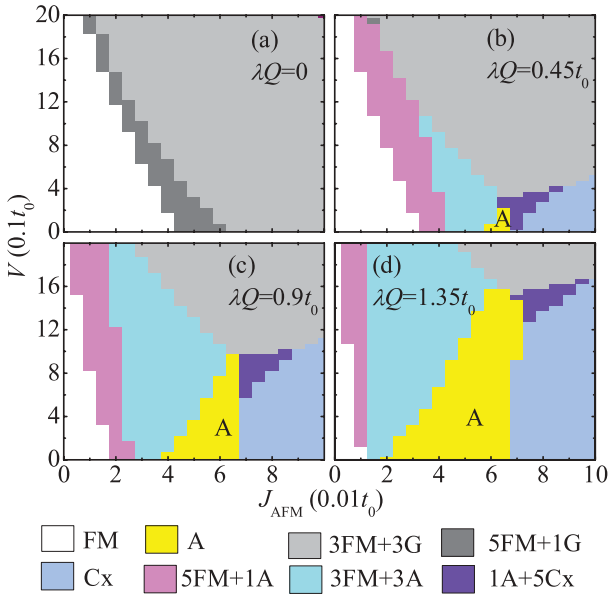

FIG. 5. (Color online) Phase diagram for the case of $(R\mathrm{MnO_3})_2/(A\mathrm{MnO_3})_4$ with $SrTiO_3$ as substrate, at several values of λQ.

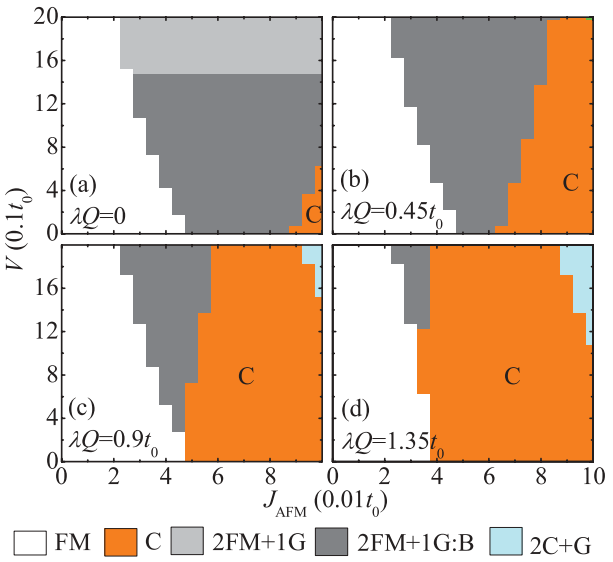

FIG. 6. (Color online) Phase diagram for the case of $(R\mathrm{MnO_3})_1/(A\mathrm{MnO_3})_2$ with $LaAlO_3$ as substrate, at several values of λQ.

G-AFM layers ($A\mathrm{MnO_3}$ layers) eventually wins in the energy competition when V is large enough, in agreement with the naive expectations presented in the introduction. However, at intermediate values of J_{AFM} and for large enough strain, represented by λQ, the experimentally observed A-AFM state is stabilized.

Increasing further J_{AFM}, the ground state becomes a Cx-type antiferromagnetic (Cx-AFM) phase. Here, the Cx-AFM is similar to the C-AFM phase, but the chains with the spins aligned lay in the a-b plane while in the standard C-AFM state this spin alignment is along the c axis (out of plane). This phase is certainly interesting but our description of results here and in the rest of the paper will focus mainly on the phases that appear at intermediate values of J_{AFM}. The reason is that for the case of bulk manganites, phases not considered in our effort such as the CE-AFM state with Q_2 distortions also appear in the range of J_{AFM} studied here, at least at particular electronic densities such as half doping. Moreover, other states stabilized at larger values of J_{AFM} and the same doping, such as the G-AFM state, have not been found experimentally for bulk compounds. Thus, it is natural that the focus of our results for superlattices should only be on the intermediate J_{AFM} range. Nevertheless, a brief discussion for narrow bandwidth manganites is presented below in this paper as well.

B. $(R\mathrm{MnO_3})_n/(A\mathrm{MnO_3})_{2n}$ on $LaAlO_3$

Consider now the case of $LaAlO_3$ as the substrate. In a recent first-principles calculation, the $(\mathrm{LaMnO_3})_n/(\mathrm{SrMnO_3})_{2n}$ superlattices grown on $LaAlO_3$ as the substrate were also studied, and results quite different from those of the $SrTiO_3$ substrate were obtained, as already mentioned in the introduction.[28] For this reason, here the phase diagrams for superlattices grown on $LaAlO_3$ are also calculated to contrast model Hamiltonian results against first-principles approaches.

In contrast to the case of $SrTiO_3$ as substrate, the lattice constant of $LaAlO_3$ (which is approximately 3.791 Å) is much smaller than the lattice constant of $R\mathrm{MnO_3}$, but it is close to $SrMnO_3$ (3.805 Å) and to $CaMnO_3$ (3.727 Å). Therefore, the $R\mathrm{MnO_3}$ layers are considerably compressed in plane while the $A\mathrm{MnO_3}$ layers are almost free from strain when $LaAlO_3$ is the substrate. Then, to simulate this strain effect a positive value of $Q_{3i} = Q$ is adopted for the $R\mathrm{MnO_3}$ layers while $Q_{3i} = 0$ is used in the $A\mathrm{MnO_3}$ region. Similarly as in the previous subsection, for the interfacial layers Q_{3i} is taken as $Q/2$ as a first-order approximation, as shown in Table I. This simple and smooth JT profile is the opposite of that used before for the $SrTiO_3$ case.

As shown in Fig. 6, the A-AFM phase, which is robust in the phase diagrams for the case of $SrTiO_3$ as substrate, no longer survives for the case of $LaAlO_3$. Instead, now the C-AFM state becomes the most likely phase appearing in reasonable regions of parameter space for the large-bandwidth manganites. This result agrees with the first-principles prediction that the C-AFM phase is quite robust in the $(\mathrm{LaMnO_3})/(\mathrm{SrMnO_3})_2$ superlattice on $LaAlO_3$.[28] Note that in Fig. 6 strain is crucial to stabilize the C-AFM phase. Without strain, the naive expectation described in the introduction of finding G-AFM layers in the $A\mathrm{MnO_3}$ region is indeed fulfill since the 2FM + 1G and 2FM + 1G:B states dominate. Once again, the crucial role of strain in these investigations becomes clear.

Note, however, that for $(R\mathrm{MnO_3})_2/(A\mathrm{MnO_3})_4$ the uniform C-AFM phase appears to be fragile and becomes stable only in a small region varying V (Fig. 7). Instead, the hybrid configuration consisting of three FM layers ($R\mathrm{MnO_3}$ and interfacial layers) plus three G-AFM layers ($A\mathrm{MnO_3}$ layers) is mainly stabilized when V increases. Thus, the experimental realization of the C-AFM state for $n = 2$ using LAO as substrate appears more problematic than for $n = 1$. Further increasing n, eventually the naive expectation of a G-AFM dominance in the $A\mathrm{MnO_3}$ region must be satisfied, but it is difficult to predict the precise value of n for the transition from

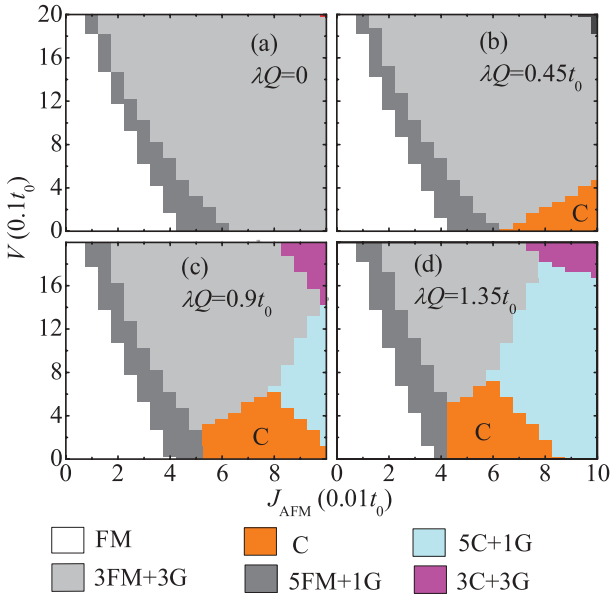

FIG. 7. (Color online) Phase diagram for the case of (RMnO$_3$)$_2$/(AMnO$_3$)$_4$ with LaAlO$_3$ as substrate, at several values of λQ.

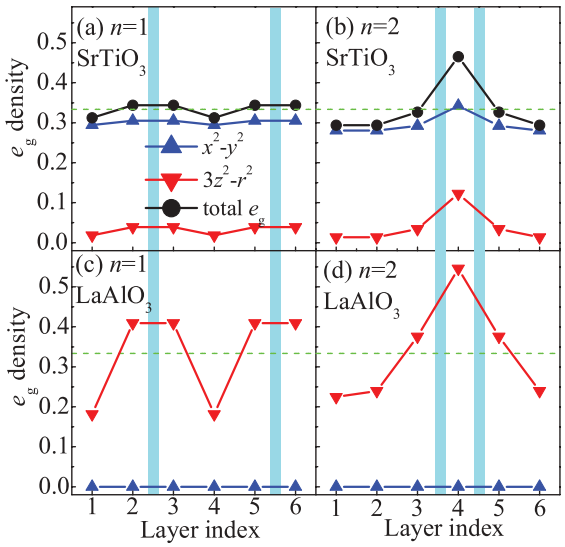

FIG. 8. (Color online) The e_g density profiles of the orbital levels in (RMnO$_3$)$_n$/(AMnO$_3$)$_{2n}$ for the special example of $V = 0.6t_0$ and $\lambda Q = 0.9t_0$. In all panels, the values of n and the substrate used are indicated. The total e_g density (black) and the orbital occupations (blue, $d_{x^2-y^2}$; red, $d_{3z^2-r^2}$) are shown. In panels (c) and (d), the $d_{3z^2-r^2}$ orbital is virtually the only occupied orbital, and for this reason the total density is not shown since it is virtually identical to the $d_{3z^2-r^2}$ density. The cyan bars denote the RO sheets in the superlattices.

a C-AFM dominated to a G-AFM dominated behavior in the AMnO$_3$ layers.

C. Electronic density and orbital occupation

The e_g electronic density and the orbital occupancies are important factors to understand intuitively the origin of the previously described ground states of the (RMnO$_3$)$_n$/(AMnO$_3$)$_{2n}$ superlattices on different substrates. These quantities are closely related to both the uniform Q_3 JT distortions (determined by the substrates) and the spin arrangements.

As a typical example, the case of $V = 0.6t_0$ and $\lambda Q = 0.9t_0$ will be discussed in detail, and the e_g electronic densities and their orbital components will be calculated explicitly. As shown in Figs. 8(a) and 8(b), for the case of the A-AFM phase on SrTiO$_3$ the e_g densities only weakly fluctuate around the average value $n_e = 1/3$ all through the six layers of the superlattice studied here, despite the presence of the electrostatic potential modulation. In fact, even the lowest e_g density within the AMnO$_3$ region is still quite robust and only slightly smaller than 0.3; that is, it is appreciably higher than the e_g electronic density of AMnO$_3$ in the bulk (i.e., ∼0). In other words, the transfer of charge from RMnO$_3$ to AMnO$_3$ in these superlattices with thin components is quite prominent and important to stabilize the particular spin orders that have been discussed in this paper. Therefore, the magnetic orders found in the present manganite superlattices cannot be simply extended to pure RMnO$_3$ and AMnO$_3$ films even under the same strain conditions.

This is a crucial observation to understand the stabilization of the A-AFM order in the superlattice as compared to the G-AFM order in the bulk of AMnO$_3$. Note that in previous theoretical studies of (LaMnO$_3$)$_{2n}$/(SrMnO$_3$)$_n$ superlattices,[25,26] the G-AFM order was found to be stable in the SrMnO$_3$ region because its local electron density was much lower than found in the example studied here. The reason for this difference is the inclusion of strain effects (i.e., a nonzero λQ) in the present analysis. In fact, the effort described here suggests that it may be necessary to revisit the previously studied (LaMnO$_3$)$_{2n}$/(SrMnO$_3$)$_n$ system, because the effects of strain were not taken into account in those previous theoretical investigations.

For the case of the C-AFM phases on LaAlO$_3$ the situation is different. In this case, the orbital occupation is purely $d_{3z^2-r^2}$, without an appreciable $d_{x^2-y^2}$ component. The e_g electronic densities are also substantially modulated, following much closer the cations than for the case of SrTiO$_3$. This charge modulation is prominent for the C-AFM phases on LaAlO$_3$, while for the A-AFM phases on SrTiO$_3$ the electronic density is almost uniform for $n = 1$ and only weakly modulated for $n = 2$, as it is clear by comparing Figs. 8(a) and 8(b) with 8(c) and 8(d).

Addressing now the orbital occupation, for the A-AFM phase on SrTiO$_3$ the $d_{x^2-y^2}$ is the orbital the most populated, with a mild contribution of the $d_{3z^2-r^2}$ component in the RMnO$_3$ portion of the superlattice for $n = 2$, as shown in Figs. 9(a) and 9(b). On the other hand, for the C-AFM phase on LaAlO$_3$, it is the $d_{3z^2-r^2}$ orbital that dominates, as intuitively expected [see Figs. 9(c) and 9(d)]. Figures 9(a)–9(d) show only one line of orbitals running perpendicularly to the interfaces because the orbital occupation is the same in all the sites of the x-y layers since the A-AFM and C-AFM are uniform in those layers.

To understand better the density and orbital profiles found in our variational study, the splitting of the energy between the two e_g orbitals induced by the Q_3 mode is shown in Figs. 10(a)–10(d). On SrTiO$_3$, the $d_{x^2-y^2}$ and $d_{3z^2-r^2}$ orbital levels in the AMnO$_3$ region of the superlattice are shifted

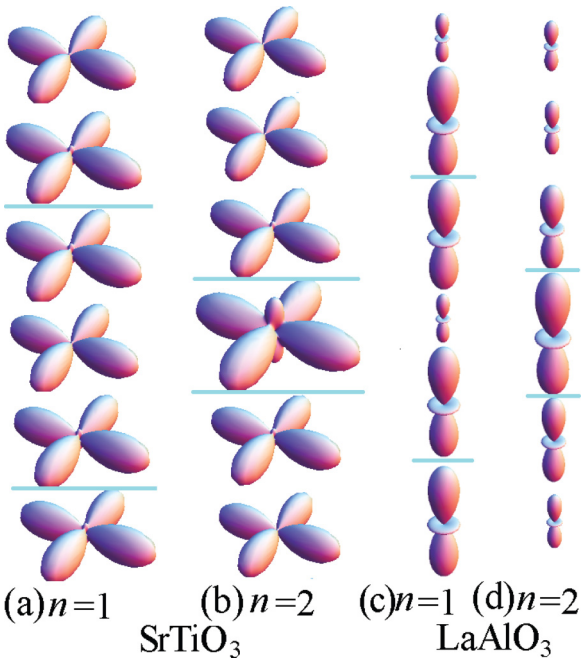

FIG. 9. (Color online) Sketch of the dominant orbital occupation for the two substrates and the two values of n studied in this paper. The six drawings for each case correspond to the six layers studied here, and their size is proportional to the actual occupation of the respective orbitals. The lines in cyan indicate where the RO layers are. Since the associated A-AFM and C-AFM magnetic orders are uniform in the layers that form the superlattice, then the results in this figure are the same for all the other chains running in the direction perpendicular to the interfaces.

down and up, respectively, due to the influence of the λQ_{3i} coupling in that region, while they are degenerate for $n = 2$ in the $R\mathrm{MnO_3}$ portion of the superlattice due to its nearly cubic lattice symmetry ($\lambda Q_{3i} = 0$ there). Note that for $n = 1$, λQ_{3i} is always nonzero, thus there is always a splitting between the two orbitals. Therefore, the $d_{x^2-y^2}$ level in the $A\mathrm{MnO_3}$ region is low enough to "accumulate" e_g electrons even when the electrostatic potential V_i is imposed, as shown in Figs. 10(a) and 10(b). Since the $d_{x^2-y^2}$ orbital, with its in-plane lobes, prefers the in-plane double-exchange hopping between NN sites, then the A-AFM state is stabilized since in this case the double-exchange process is precisely restricted to occur within the x-y plane.

Contrary to the case of $SrTiO_3$, when $LaAlO_3$ is the substrate the $d_{x^2-y^2}$ and $d_{3z^2-r^2}$ orbital levels in the $R\mathrm{MnO_3}$ portion of the superlattice are shifted up and down, respectively, due to the influence of λQ_{3i}, while they are degenerate in the $A\mathrm{MnO_3}$ component of the superlattice where $\lambda Q_{3i} = 0$. Since the double-exchange process in the C-AFM phase is only active along the out-of-plane chains with the same orientation of the spin and since in this direction the hoppings associated with $x^2 - y^2$ vanish ($t^z_{aa} = t^z_{ba} = t^z_{ab} = 0$), then the $d_{3z^2-r^2}$ orbital is occupied while the $d_{x^2-y^2}$ orbital is virtually empty.

In summary, the two e_g orbitals are both active in unstrained layers but typically only one dominates in the uniformly strained layers. This simple observation is sufficient to understand several features of the phase diagrams that were obtained numerically.

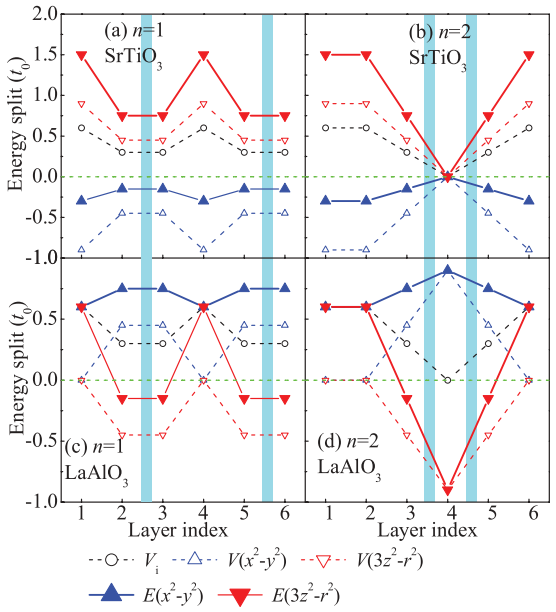

FIG. 10. (Color online) The e_g-orbital energy splitting and the electrostatic potentials in $(R\mathrm{MnO_3})_n/(A\mathrm{MnO_3})_{2n}$ for the special example of $V = 0.6t_0$ and $\lambda Q = 0.9t_0$. In all panels, the values of n and the substrate used are indicated. The final energy levels of the two orbitals (after the JT splitting plus the shift from V_i) are shown as the blue ($d_{x^2-y^2}$) and red ($d_{3z^2-r^2}$) solid curves. The cyan bars denote the RO sheets in the superlattices. The electrostatic potentials V_i are shown in dashed black curves. For completeness, the energy split of the two orbitals only due to the JT Q_3 mode is also shown, with the blue (red) dashed curve denoting the $d_{x^2-y^2}$ ($d_{3z^2-r^2}$) orbital.

D. Extensions to narrow-bandwidth manganite superlattices

Most experiments on Mn-oxide superlattices have focused on the wide-bandwidth manganites involving $LaMnO_3$ and $SrMnO_3$ as components.[13–19,21,24] For this reason considerable theoretical investigations have been carried out with this focus as well.[25,26,28] However, some recent theoretical efforts pointed out that exotic phenomena might exist at interfaces involving narrow-bandwidth manganites, even including the presence of novel magnetic states that do not appear in the bulk phase diagrams of the individual materials that form the superlattice.[35] Since reducing the bandwidth is equivalent to increasing the values of J_{AFM} and V, because they are in units of the hopping t_0, then the previously discussed phase diagrams contained in Figs. 4–7 indicate that other magnetic orders beyond the uniform A-AFM and predicted C-AFM states could be stabilized in these superlattices if the parameters J_{AFM} or V are increased further by using manganites different from $LaMnO_3$ or $SrMnO_3$.

For example, considering the case of the $SrTiO_3$ substrate, the uniform Cx-AFM order is neighboring the A-AFM order in the phase diagrams in Figs. 4 and 5, and it appears to be quite robust in both the $n = 1$ and $n = 2$ superlattices for a sufficiently large J_{AFM} (corresponding to narrow-bandwidth cases). It should be noted that the Cx-AFM order does *not* exist in bulk form, thus its stabilization in superlattices would be quite interesting. The Cx-AFM phase, which breaks the in-plane symmetry between the two directions, will result in macroscopic physical anisotropies in, for example,

transport properties even when the underlying substrate is cubic.

The phase diagrams for the case of $SrTiO_3$ as substrate include several other phases besides the A-AFM and Cx-AFM states. These other phases correspond to combinations of FM, A-AFM, and G-AFM states, with different patterns, as shown in Figs. 4 and 5. For configurations involving a FM component, note that it is quite difficult to obtain a macroscopic magnetization in these superlattices, since there is no place for FM order in the phase diagrams for manganites when in bulk form and for hole doping $x > 0.5$.[27,37] Thus, if a net magnetic moment could be stabilized via superlattices for a nominal composition x larger than 0.5, this would also represent a new state that is not present in bulk form. Moreover, combinations of FM and G-AFM layers could potentially be used as spin valves by controlling the local magnetic orders with magnetic fields.

With regards to the $LaAlO_3$ substrate, the C-AFM state is quite robust in the $n = 1$ case (Fig. 6), which may imply an enhanced Néel temperature, analogous to the enhanced A-AFM Néel temperature observed experimentally for $SrTiO_3$ as substrate. However, in the $n = 2$ case the C-AFM state occupies a smaller portion of the phase diagram and states such as those involving thre FM layers plus three G-AFM layers may become stable if V is increased further, similarly as in the case using $SrTiO_3$. Other combinations such as the five C-AFM layers plus one G-AFM layer are also possible if the bandwidth is reduced. In this case, and also for $SrTiO_3$, the phase diagrams are rich, implying states that are very close in energy, and it is possible that external magnetic fields could be used to tune the ground-state properties of these superlattices.

IV. SUMMARY

Summarizing, here the two-orbital double-exchange model was employed to investigate the phase diagrams of the (RMnO$_3$)$_n$/(AMnO$_3$)$_{2n}$ superlattices. Two different substrates have been tested to illustrate two different types of strain effects, giving rise to distinct ground states and phase diagrams. The underlying dominant physical mechanism is the non-uniform splitting of the e_g orbital levels by the Q_3 mode of Jahn-Teller distortion imposed by the substrate strain. Besides the uniform A-type and C-type antiferromagnetic phases that are stabilized in the intermediate range of couplings for the case of the wide-bandwidth manganite superlattices, our study also reveals several other possible phases, including many with nonuniform modulations of the spin order. These exotic patterns could be found in superlattices built using narrow-bandwidth manganites, an area of research that should be more actively pursued experimentally due to its potential to unveil new states of manganites.

ACKNOWLEDGMENTS

This Work was supported by the 973 Projects of China (2011CB922101), NSFC (11004027, 11274060, 11234005), NCET, and RFDP. Q.F.Z. was supported by NSFC (11204265), the NSF of Jiangsu Province (BK2012248), and research fund of Key Laboratory for Advanced Technology in Environmental Protection of Jiangsu Province (AE201125). Q.F.Z. and S.Y. were supported by CREST-JST. The work of E.D. for this project was supported by the US Department of Energy, Office of Basic Energy Sciences, Materials Sciences and Engineering Division.

[1] J. Mannhart and D. G. Schlom, Science **327**, 1607 (2010).
[2] H. Takagi and H. Y. Hwang, Science **327**, 1601 (2010).
[3] G. Hammerl and N. Spaldin, Science **332**, 922 (2011).
[4] H. Y. Hwang, Y. Iwasa, M. Kawasaki, B. Keimer, N. Nagaosa, and Y. Tokura, Nat. Mater. **11**, 103 (2012).
[5] E. Dagotto, Science **318**, 1076 (2007).
[6] M. Bibes, J. E. Villegas, and A. Barthélémy, Adv. Phys. **60**, 5 (2011).
[7] L. W. Martin, Y.-H. Chu, and R. Ramesh, Mater. Sci. Eng., R **68**, 89 (2010).
[8] J. Chakhalian, J. W. Freeland, H.-U. Habermeier, G. Cristiani, G. Khaliullin, M. V. Veenendaal, and B. Keimer, Science **318**, 1114 (2007).
[9] C. Visani, Z. Sefrioui, J. Tornos, C. Leon, J. Briatico, M. Bibes, A. Barthélémy, J. Santamaría, and J. E. Villegas, Nat. Phys. **8**, 539 (2012).
[10] W. S. Choi, D. W. Jeong, S. S. A. Seo, Y. S. Lee, T. H. Kim, S. Y. Jang, H. N. Lee, and K. Myung-Whun, Phys. Rev. B **83**, 195113 (2011).
[11] M. Gibert, P. Zubko, R. Scherwitzl, J. Íñiguez, and J.-M. Triscone, Nat. Mater. **11**, 195 (2012).
[12] S. W. Wu, S. A. Cybart, P. Yu, M. D. Rossell, J. X. Zhang, R. Ramesh, and R. C. Dynes, Nat. Mater. **9**, 756 (2010).
[13] T. Koida, M. Lippmaa, T. Fukumura, K. Itaka, Y. Matsumoto, M. Kawasaki, and H. Koinuma, Phys. Rev. B **66**, 144418 (2002).
[14] A. Bhattacharya, X. Zhai, M. Warusawithana, J. N. Eckstein, and S. D. Bader, Appl. Phys. Lett. **90**, 222503 (2007).
[15] Ş. Smadici, P. Abbamonte, A. Bhattacharya, X. Zhai, B. Jiang, A. Rusydi, J. N. Eckstein, S. D. Bader, and J.-M. Zuo, Phys. Rev. Lett. **99**, 196404 (2007).
[16] C. Adamo, X. Ke, P. Schiffer, A. Soukiassian, W. Warusawithana, L. Maritato, and D. G. Schlom, Appl. Phys. Lett. **92**, 112508 (2008).
[17] C. Adamo, C. A. Perroni, V. Cataudella, G. De Filippis, P. Orgiani, and L. Maritato, Phys. Rev. B **79**, 045125 (2009).
[18] A. Bhattacharya, S. J. May, S. G. E. te Velthuis, M. Warusawithana, X. Zhai, B. Jiang, J.-M. Zuo, M. R. Fitzsimmons, S. D. Bader, and J. N. Eckstein, Phys. Rev. Lett. **100**, 257203 (2008).
[19] S. J. May, A. B. Shah, S. G. E. te Velthuis, M. R. Fitzsimmons, J. M. Zuo, X. Zhai, J. N. Eckstein, S. D. Bader, and A. Bhattacharya, Phys. Rev. B **77**, 174409 (2008).
[20] A. Perucchi, L. Baldassarre, A. Nucara, P. Calvani, C. Adamo, D. G. Schlom, P. Orgiani, L. Maritato, and S. Lupi, Nano Lett. **10**, 4819 (2010).
[21] S. J. May, P. J. Ryan, J. L. Robertson, J.-W. Kim, T. S. Santos, E. Karapetrova, J. L. Zarestky, X. Zhai, S. G. E. te Velthuis,

J. N. Eckstein, S. D. Bader, and A. Bhattacharya, Nat. Mater. **8**, 892 (2009).
[22]A. Galdi, C. Aruta, P. Orgiani, C. Adamo, V. Bisogni, N. B. Brookes, G. Ghiringhelli, D. G. Schlom, P. Thakur, and L. Maritato, Phys. Rev. B **85**, 125129 (2012).
[23]H. Yamada, P.-H. Xiang, and A. Sawa, Phys. Rev. B **81**, 014410 (2010).
[24]E. J. Monkman, C. Adamo, J. A. Mundy, D. E. Shai, J. W. Harter, D. Shen, B. Burganov, D. A. Muller, D. G. Schlom, and K. M. Shen, Nat. Mater. **11**, 855 (2012).
[25]S. Dong, R. Yu, S. Yunoki, G. Alvarez, J.-M. Liu, and E. Dagotto, Phys. Rev. B **78**, 201102(R) (2008).
[26]B. R. K. Nanda and S. Satpathy, Phys. Rev. B **79**, 054428 (2009).
[27]Y. Tokura, Rep. Prog. Phys. **69**, 797 (2006).
[28]Q. F. Zhang, S. Dong, B. L. Wang, and S. Yunoki, Phys. Rev. B **86**, 094403 (2012).
[29]Z. Fang, I. V. Solovyev, and K. Terakura, Phys. Rev. Lett. **84**, 3169 (2000).
[30]B. R. K. Nanda and S. Satpathy, Phys. Rev. B **78**, 054427 (2008).
[31]E. Dagotto, T. Hotta, and A. Moreo, Phys. Rep. **344**, 1 (2001).
[32]E. Dagotto, *Nanoscale Phase Separation and Colossal Magnetoresistance* (Springer, Berlin, 2002).
[33]E. Dagotto, J. Burgy, and A. Moreo, Solid State Commun. **126**, 9 (2003).
[34]B. R. K. Nanda and S. Satpathy, Phys. Rev. B **81**, 224408 (2010).
[35]R. Yu, S. Yunoki, S. Dong, and E. Dagotto, Phys. Rev. B **80**, 125115 (2009).
[36]T. Hotta, S. Yunoki, M. Mayr, and E. Dagotto, Phys. Rev. B **60**, R15009 (1999).
[37]J. Hemberger, A. Krimmel, T. Kurz, H.-A. Krug von Nidda, V. Y. Ivanov, A. A. Mukhin, A. M. Balbashov, and A. Loidl, Phys. Rev. B **66**, 094410 (2002).
[38]G. Bouzerar and O. Cépas, Phys. Rev. B **76**, 020401(R) (2007).
[39]J. Salafranca, G. Alvarez, and E. Dagotto, Phys. Rev. B **80**, 155133 (2009).
[40]S. Dong, X. Zhang, R. Yu, J.-M. Liu, and E. Dagotto, Phys. Rev. B **84**, 155117 (2011).
[41]S. Dong, R. Yu, S. Yunoki, J.-M. Liu, and E. Dagotto, Phys. Rev. B **78**, 064414 (2008).
[42]S. Dong, X. Y. Yao, K. F. Wang, and J.-M. Liu, J. Phys.: Condens. Matter **18**, L171 (2006).
[43]J. A. Alonso, M. J. Martínez-Lope, M. T. Casais, and M. T. Fernández-Díaz, Inorg. Chem. (Washington, DC, US) **39**, 917 (2000).
[44]O. Chmaissem, B. Dabrowski, S. Kolesnik, J. Mais, D. E. Brown, R. Kruk, P. Prior, B. Pyles, and J. D. Jorgensen, Phys. Rev. B **64**, 134412 (2001).